A Methodology for Manufacturing 3D Disordered Metamaterials Using Laser Powder Bed Fusion from Granular Packings and Hyperuniform Point Clouds

Katherine Moody[a], Molly Li[b], Charles Emmett Maher[c], Kwangmin Lee[d], Tim Horn[a], Katherine A. Newhall[c], Ryan Hurley[e], Karen E. Daniels[f], Christopher Rock*[g]

[a]*Department of Mechanical Engineering, North Carolina State University, Raleigh, NC, USA*
[b]*Master of Engineering Management, North Carolina State University, Raleigh, NC, USA*
[c]*Department of Mathematics, University of Chapel Hill, Chapel Hill, NC, USA*
[d]*Department of Mechanical Engineering, Johns Hopkins University, Baltimore, MD, USA*
[e]*Department of Mechanical Engineering, Hopkins Extreme Materials Institute, Johns Hopkins University, Baltimore, MD, USA*
[f]*Department of Physics, North Carolina State University, Raleigh, NC, USA*
[g]*Center for Additive Manufacturing and Logistics, North Carolina State University, Raleigh, NC, USA*

---

*Corresponding Author.
kmoody@ncsu.edu
412-328-7304
915 Partners Way, Room 2200
Raleigh, NC, 27607

1. Abstract

Three-dimensional open geometries originating from nontraditional manufacturing designs such as point clouds, sphere packings, and mathematical file generation can be challenging to manufacture when the structures have disorder and overhanging geometric features. This study algorithmically created rigid 3D geometries representing granular packings and hyperuniform point clouds suitable for fabricating metallic disordered metamaterial (MDM) geometries using additive manufacturing. This approach produced nonrepeating connecting beam angles ranging from 0° to 90° relative to the build plate. Prototyping using laser powder bed fusion (LPBF) was challenging for the low-angle connecting beams, due to heat transfer differences when printing on powder compared with a solid substrate. An initial set of unsupported MDM geometries revealed failed connecting beams and geometric inaccuracy. We performed a systematic study to emulate the complex beam angles by printing cylinders ranging from 1.0 mm to 3.0 mm in diameter and angles ranging from 10°, to 90°, relative to the build plate. Unsupported connecting beams tended to lose geometric integrity at angles below 30°, and failed at 10°, resulting in geometric deviation on the downfacing surfaces. However, varying LPBF input energies and support strategies mitigated the geometric deviation. These results were used to successfully fabricate MDM geometries with limited and removable supports.

2. Introduction

Open lattices, complex systems, and repeating cell metamaterials have gained attention as engineering materials due to their high strength-to-weight ratio and tunable transport, optical, and mechanical properties [1, 2, 3, 4, 5, 6, 7]. Among these, disordered hyperuniform systems are of specific interest, as they have mathematically demonstrated properties ranging from tunable elastic moduli, complete isotropic photonic band gaps, resistivity, and enhanced absorption of acoustic and electromagnetic waves [8, 9, 10, 11, 12]. Disordered hyperuniform systems are characterized by an anomalous suppression of large-scale density fluctuations compared to those found in standard disordered systems [13, 14]. The hyperuniformity of a sample can be diagnosed via, e.g., X-ray scattering experiments if the scattering intensity $S(\mathbf{k})$ of the sample approaches zero as the wavenumber $k \equiv |\mathbf{k}|$ tends to zero, ignoring forward scattering [15], i.e., $S(k) \rightarrow 0$ as $k \rightarrow 0$. Hyperuniform density fluctuations can be found in a wide variety of different systems including biological [16, 17, 18], astrophysical [19, 20], and packings of spherical [21, 22, 23, 24, 25, 26] and nonspherical [27, 28, 29] particles, among many others (see. e.g., Ref 14 for additional examples). However, these systems offer considerable challenges to manufacture into engineering structures due to their nontraditional geometries, which may contain multiple connecting beams at aperiodic angles and variations in beam density and diameter. Additionally, limited studies exist for fabricating open hyperuniform systems as solid geometries, especially in common engineering alloy systems such as titanium (Ti), steels, or nickel (Ni) alloys.

Many approaches exist to computationally generate and study hyperuniform structures, to expand the design space available for solid geometries [30, 31, 1, 9, 32, 33, 34]. An extensive review of such methods can be found in Refs. 14, 35, and references therein. Often, these methods result in a dispersion of disjoint bodies, e.g., the scheme in Ref. 30 that describes a tessellation-based scheme to make polydisperse hyperuniform dispersions of nonoverlapping particles, making it difficult to construct them experimentally. A promising method for converting such computer-generated hyperuniform point clouds into manufacturable geometries is to generate a tessellation from the point cloud and then use the resulting set of line segments [36, 9, 37, 38] as printable beams. For example, Muller et al. [39] designed a 3D cellular geometry by connecting centroids of hyperuniform sphere packings to create a disordered network of beams. However, manufacturing of engineered hyperuniform-inspired materials has mostly been limited to singular custom assemblies due to the inherent complexity of the structure and finite scale effects [40, 41]. Namely, Chéron et al. [42] arranged alumina beams in a hyperuniform point pattern to study wave transport [42], and Man et al. [36] constructed a hyperuniform disordered network of cells comprised of alumina cylinders and walls to study photonic band gaps. Moreover, computational studies of these network structures generated from hyperuniform point clouds demonstrated their desirable conductive and elastic properties [9, 37, 38].

Additive manufacturing (AM) opens up new opportunities to produce disordered and complex structures because the layer-by-layer nature of the process allows for geometric freedom and the fabrication of highly complex geometries [43, 44, 45]. Furthermore, AM offers flexibility in materials selection and size scale, making this process suitable for hyperuniform and disordered materials discovery [46]. A limited number of studies have reported the use of AM to fabricate solid geometries from granular and hyperuniform-inspired structures. Siedentop et al. [47] manufactured a stealthy hyperuniform 3D geometry using selective laser sintering (SLS) of Nylon mixed with high refractive index additives to explore bandgap structure response. Sniechowski et al. [48] used a hyperuniform point cloud to represent trabecular bone, using network theory techniques to connect point clouds into an STL file for 3D printing. Demonstration articles of the bone with a 5 mm footprint were produced using digital light processing (DLP) of resin and laser powder bed fusion (LPBF) of Ti-6Al-4V, and Wit et al. [49] performed a similar experiment using DLP of resin. Muller et al. [39] used a related DL-writing (DLW) AM process using resin with TiO_2 and chemical vapor deposition of Si to form hyperuniform microlattices to study photonic band gap materials. Although these reported examples demonstrated that AM of hyperuniform-inspired solid materials is possible, a manufacturing methodology remains undeveloped for fabricating metallic disordered metamaterial (MDM) geometries using common engineering metals and alloys.

PBF processes are well-established methods for producing metal parts by AM [43, 44]. Inherent process parameters, such as laser or electron beam spot size and powder size distribution, enable the fabrication of high-precision, submillimeter scale features, often utilized in the manufacturing of repeating cell metamaterials and lightweight lattice structures [50, 51, 52]. Fewer works have explored AM as an avenue for fabricating stochastic lattice structures, largely focused on trabecular design for biomedical applications [53, 54, 55, 56, 57, 58, 59]. Other approaches have been developed to generate different types of stochastic lattice networks for AM, including a strut based cancellous bone-inspired stochastic network [60], a Poisson Disk algorithm distribution of connected nodes [61], and heterogeneous unit cells of square grids with diagonal struts inspired by glass sponges [62]. Despite these advancements, there remain limitations in this body of work. For example, a majority of these studies fabricated the lattices in Ti-6Al-4V, which has well known material properties and process parameters [63, 54, 55, 62, 61, 59, 64], with only a few studies exploring different material systems, such as magnesium [65], tantalum [53, 66, 56, 61], and NiTi [58]. Additionally, many of the studies show the ability to fabricate complex lattice structures, but fail to quantitatively address the quality of the manufactured parts. In light of these aspects, a compelling next step is to combine the robust research on LPBF of metamaterial and stochastic lattice structures [67, 68, 51] with hyperuniform exploration, resulting in a new class of disordered metamaterials. This new class of disordered metamaterials differ from previously studied stochastic lattices, in that the structures contain long range uniformity despite the random appearance, allowing for predictable and tunable properties compared to the stochastic counterparts. However, introducing geometric disorder into metamaterials, such as nonrepeating cells, aperiodic beam angles, and varying connecting beam diameters, raises unique challenges pertaining to LPBF. These include features such as overhang angles [69, 70, 71, 72], thin walls [73, 74], and support design.

As previously discussed, limited material systems are reported for AM of stochastic lattices or hyperuniform geometries. Therefore we selected the copper-based alloy, GRCop-42 due to its combination of transport and tunable mechanical properties which are of great interest for hyperuniform systems. GrCop-42 is an alloy developed at NASA Glenn Research Center designed for applications such as, thin-walled regeneratively cooled combustion chambers in rockets, which require material capable of high heat flux, oxidation resistance and elevated temperature strength[75, 76, 77, 78, 79, 80, 81]. The alloy was one of a series of high heat flux materials with generic compositions of Cu-2Cr-Nb (4Cr-2Nb for GrCop-42) which forms nanoscale Cr_2Nb as an intermetallic strengthener. GrCop-42 has been reported to have thermal conductivity exceeding 300 W/mK at 1000K and electrical conductivity approaching 85% of the international standard for annealed copper (IACS), while maintaining an ultimate tensile strength of 150 MPa at 750K. This combination of properties makes it interesting to study for hyperuniform systems with potentially unique transport, such as tunable heat transfer & electrical resistivity and high strength-to-weight ratio geometries. This alloy was traditionally gas atomized into powder to avoid coarsening of the intermetallic, and consolidated by conventional low temperature powder metallurgy (P/M) operations such as warm rolling or forging. Recently the alloy has been processed by LPBF to take advantage of the fast cooling rates associated with melt pool solidification to maintain fine Cr_2Nb dispersoids.

Our study focuses on developing a systematic, material agnostic, and geometrically accurate manufacturing process to fabricate complex MDM geometries, overcoming many of the challenges existing in the current literature. First we generate a ”math to STL” pipeline, taking disjointed point clouds and connecting them to make printable geometries. In doing so, we expand the capability of creating hyperuniform materials from singular custom assemblies to manufacturable parts. Second, we provide a systematic method for developing successful process parameters required to print geometrically accurate MDM geometries. This process is intended for iterative design where geometric accuracy is critical to maintain and quantify hyperuniformity. This method is material agnostic, extending the range of potential alloys that can be used for LPBF of these complex components. Finally, we present analysis techniques to quantify geometric error in the MDM geometries, and show the role of varying process parameters and supports on geometric accuracy.

3. Methods

3.1. Disordered Geometry Generation

Figure 1 illustrates the steps to convert the granular configuration and hyperuniform point clouds into printable STL files. The granular configurations start as output from the molecular dynamics software LAMMPS [82], where a point cloud was created containing the locations of the centers of the spheres and an adjacency matrix listing all particles, which were recorded with non-zero force [11]. A round beam was created for each such interparticle contact, and the beams were assembled into a nominal geometry and output to an STL file for AM [83]. The code-generated STL file was then input into Materialize Magics for minor repair prior to LPBF.

The hyperuniform point cloud considered in this work is the uniformly randomized lattice (URL) [84]. To generate a URL point cloud, a set of $N = n^3$ points were arranged in a simple cubic lattice, where n is the number of points along one of the axes of the periodic simulation box. Each point was then displaced in this lattice by a 3-dimensional vector where each element of the vector was uniformly randomly chosen from the interval $\left[-\frac{a}{2}, \frac{a}{2}\right)$, where the perturbation strength a is given in units of the size of the simple cubic fundamental cell. This type of point cloud has $S(k) \sim k^2$ scaling as $k \to 0$ for all values of $a > 0$, and thus is in the strongest class of hyperuniformity [84]. In this work we chose $N = 216$ and $a = 0.1$ and 1.0. To convert these point cloud into a network structures a Voronoi tessellation was computed by finding the region of space that was closest to each point in the point cloud (respecting periodic boundary conditions), which yielded a set of polyhedra that filled the simulation box. The set of edges that made up each polyhedron was the set of edges that was then treated as the network. It should be noted here that while the point cloud considered here is hyperuniform, the corresponding network only partially inherited the hyperuniformity of the progenitor point cloud [85]. To convert this network into a printable structure, the structure was truncated at the periodic boundaries and each edge replaced by a cylinder, the union of which was output to an STL file for AM.

3.2. Materials and Additive Manufacturing

All metallic articles were manufactured using 15 to 45 micron GRCop-42 powder on an EOS M290 with a constant 0.03 mm layer thickness and a 0.080 mm laser spot diameter. First, a design of experiment was conducted using 10 mm × 10 mm × 10 mm cubes fabricated with varying laser power, speed, and hatch to develop a parameter set resulting in 99.9% density, referred to as ”standard” in Table 1.

Cylinders of 3.0, 2.0, and 1.0 mm in diameter and 10 mm in length were fabricated on a rectangular base of 5 mm × 8 mm × 30 mm to study the effect of print angles on geometric integrity. The cylinders were printed at angles of 90°, 60°, 30°, and 10°, respectively, to the build plate to emulate the range of angles observed in the MDM STL file, as demonstrated in Figure 1c and f. The cylinders were designed using Materialize Magics and printed with a standard and a reduced energy parameter set for both melt and downskin parameters. The downskin

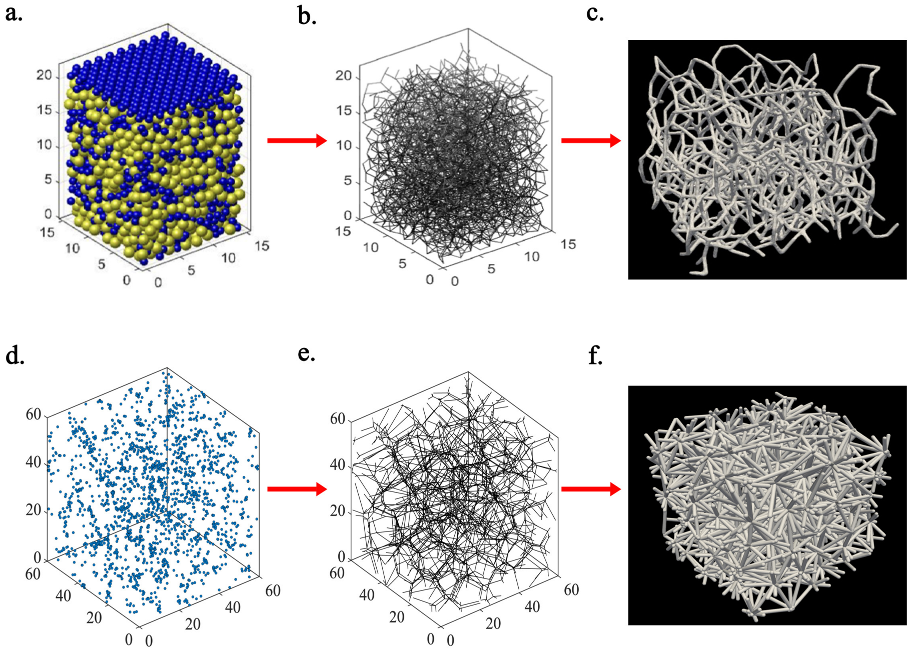

Figure 1: *(a)* Rendering of a granular packing created in LAMMPS by raining particles under gravity, together with the force network *(b)* observed within that packing [11], *(c)* rendering of an STL File generated from an example force network. *(d)* Rendering of a hyperuniform point cloud, connected by an adjacency matrix to form a network *(e)*, and *(f)* rendering of an STL file generated from the hyperuniform point cloud. Images for *(a)* and *(b)* are reproductions with permission from Springer Nature.

was applied to the entirety of the first 3 layers of the overhanging geometries below 40 degrees, before the melt parameters began. Selected parameters used in the experiments are shown in Table 1.

Based on the best results from the melt and downskin study, a set of 2.0 mm cylinders were fabricated at 10° with a custom support strategy to further improve the geometric accuracy of the overhanging connecting beams. The custom support design used for the cylinders and the final MDM geometries was derived from a series of experiments exploring various support types, parameters, and placement. Initial supports were generated on a full granular MDM geometry, using traditional tree & branch and polyline perforated support types. Support parameters such as distance between points of contact on the geometry surface (anchor distance), the width of the contact points (anchor width), and creation and width of breaking points in the supports were varied to examine the dynamic between ease of support removal and efficacy of supports on geometric integrity of the connecting beams. The supports were generated from the base of the plate to the connecting beams which led to difficulties in removing the support without causing damage to the connecting beams, particularly toward the center of the MDM geometry.

A new support strategy was tested using contoured area to bar supports to ease support removal. The area to bar design allows for many anchor points to be placed on each connecting beam for added support, while thin enough for easy removal. This is especially important for MDM geometries with a high density of points in the point cloud, as exterior beams limit access to internal geometries for manual support removal. The new support designs were tested on a quarter of the hyperuniform MDM geometries and 2.0 mm cylinders to compare support removal and geometric integrity of the beams. A total of 10 support designs were tested, varying anchor distance, anchor width at the connecting beams (width at end), width at platform, and breaking point width, examples of which can be seen in Figure 2. The anchor width at end was kept smaller than the breaking point width for all designs, so that the supports would break off directly at the point of contact with the connecting beams. Additionally for the quarter MDM geometries, the supports were generated from beam to beam rather than from the base of the plate to minimize the amount of support. The supports were removed from the quarter MDM geometries using a high velocity water jet to accelerate the removal process and reach all of the internal supports within the geometry.

A final set of granular and hyperuniform MDM geometries were fabricated with a nominal footprint size of 65 mm × 65 mm × 65 mm and a connecting beam diameter of 1.5 mm, both supported and unsupported for comparison. All STL files were sliced to 0.030 mm layer thickness in Materialize Magics software and all metal geometries were separated from the build plate using a Mitsubishi FA10S electrical discharge machine (EDM).

260 W Standard	Melt	Laser Power	260	W
		Laser Speed	760	mm/s
		Hatch	0.07	mm
		Energy	162.9	J/mm^3
	Original Downskin	Laser Power	86.7	W
		Laser Speed	621.5	mm/s
		Hatch	0.064	mm
		Energy	72.7	J/mm^3
220 W Reduced	Melt	Laser Power	220	W
		Laser Speed	750	mm/s
		Hatch	0.07	mm
		Energy	139.7	J/mm^3
	Reduced Original Downskin	Laser Power	73.3	W
		Laser Speed	613.3	mm/s
		Hatch	0.064	mm
		Energy	62.6	J/mm^3
Standard, Reduced	Downskin1	Laser Power	96.0	W
		Laser Speed	650.0	mm/s
		Hatch	0.07	mm
		Energy	68.1	J/mm^3
Standard, Reduced	Downskin2	Laser Power	126.0	W
		Laser Speed	650.0	mm/s
		Hatch	0.07	mm
		Energy	92.3	J/mm^3
Standard, Reduced	Downskin3	Laser Power	147.0	W
		Laser Speed	650.0	mm/s
		Hatch	0.07	mm
		Energy	107.7	J/mm^3

Table 1: GRCop-42 Machine Parameters used for the MDMs and cylinders. A 5.0 mm stripe was used for all specimens. Standard, Reduced indicates both 260 W and 220 W melt parameters were used with each respective Downskin parameter set.

3.3. *Characterization and Testing*

The 3.0, 2.0, and 1.0 mm diameter cylinders were scanned using an Amatek Creaform HandyScan 3D laser scanner with 0.025 mm resolution. The original STL files and laser scans were imported into Cloud Compare software for geometric analysis [86]. The STL files and laser scans were aligned to a root mean square (RMS) difference of 1E-7, and the distance of the vertices between the two files was calculated for geometric accuracy. This measurement method was not used on the printed disordered geometries, due to a lack of depth penetration on larger footprints.

Selected MDM geometries were examined by X-ray computed tomography (XRCT) using an RX Solutions EasyTom 150/160 micro-CT system (150 kV source). Imaging resolution was 77 m/voxel. Each geometry was fully captured within the field-of-view of its CT scan. XRCT reconstructions were performed in the RX Solutions X-Act software (version 23.04), and the reconstructed images were binarized with a fixed, heuristically chosen threshold to isolate pixels representing solid material from pixels representing voids. The binarized XRCT data was exported in 16-bit TIFF image format. The images were imported into Dragonfly software (Object Research Systems, Inc, Montreal, Quebec, Canada), where they were converted to mesh files and exported as STL files. The measured and nominal STL files were imported into Cloud Compare software [86] for geometric comparison of the fabricated and nominal MDM geometries.

3.4. *Thermal Model*

A thermal model was used to estimate melt pool temperatures during fabrication of the MDM beams. Python scripts defining the model size, boundary conditions, thermophysical properties, and process conditions (beam power, speed, and hatch, etc) were run in the open source finite element method software, FENICS [87, 88, 89, 90]. The model implemented a moving Gaussian heat source with a spot diameter of 0.080 mm to emulate the laser beam size of the EOS M290. The beam was moved in a bi-directional raster pattern with a minimum of three beam raster lines were run with a hatch spacing of 0.07 mm, depending on the parameters being evaluated. The

b.

Anchor Distance (mm)	1.13	1.38	1.38
Width at Platform (mm)	0.30	0.30	0.30
Width at End (mm)	0.025	0.050	0.25
Break Point Width (mm)	0.10	0.10	0.30

Figure 2: *(a)* Quarter hyperuniform MDM geomtries printed with varied support strategies, *(b)* Table of support parameters for each of the support strategies.

thermal model did not include fluid dynamics or change of state but has been shown to adequately describe melt pool formation in powder bed fusion [91, 92]. The pool size was estimated by sectioning the model output and applying temperature contours using Paraview [93]. The width, depth, and temperature of the melt pools were estimated by thresholding the temperature using 1356°C as liquidus.

4. Results & Discussion

Table 1 is a summary of the melt parameters used to fabricate the MDM geometries and cylinders which includes: laser power, speed, hatch, and calculated volumetric energy density[94, 95]. The standard parameters were developed using the design of experiment described in the methods demonstrating 99+% relative density. The 'Reduced' parameters represent 0.85× the laser power with a slightly adjusted speed from 760 mm/s to 750 mm/s to account for the lower power. It is common in LPBF parameter development studies to use prismatic shapes such as cubes, cylinders, thin wall plates, or hollow tubes [96, 97, 98, 73, 99]. However, when printing MDM geometries, each 2D slice of the STL file produces an unorthodox and aperiodic melt pattern which results in random local and global heat input for each layer. The irregular heat input makes the implementation of a single parameter set difficult, so the application of melt and downskin parameters, plus removable supports, is important for parameter development of these structures.

Figure 3a is a post-melt image of a typical aperiodic melted layer, where low-angle beams printed as long surfaces, often exhibiting oxidation and tinting due to overheating as indicated by the red arrows. This occurs especially in the first few layers of the beams below 30°, as each horizontal beam extends its length over powder for a given layer. In contrast, angles exceeding 75° print as round areas where the heat extraction is comparable to that of prismatic articles. Figure 3b shows two resulting AM-fabricated, unsupported MDMs with varying structural disorder (left to right, a=0.1 & a=1.0), and multiscale disorder such as beam surface roughness and powder particle adherence which are of interest, because the transport properties in some systems may be influenced by multiscale disorder [14]. For PBF, the influence of size scale will become nontrivial at diameters below 0.5 mm, due to the convergence of feedstock particle and melt pool sizes with small diameter connecting beam dimensions.

A general inspection of the unsupported geometries in Figure 3 shows largely successful prints. However, close inspection reveals a number of connecting beams have obvious geometrical defects, including powder agglomerations, severe warping, or failure below 30°, typical of reported overhang features in LPBF. One method to reduce geometric defects in overhanging structures is the use of downskin parameters. Cylinders ranging in diameter from 1.0 to 3.0 mm were printed at angles from 10° to 90° using 260 W and 220 W melt parameters, as

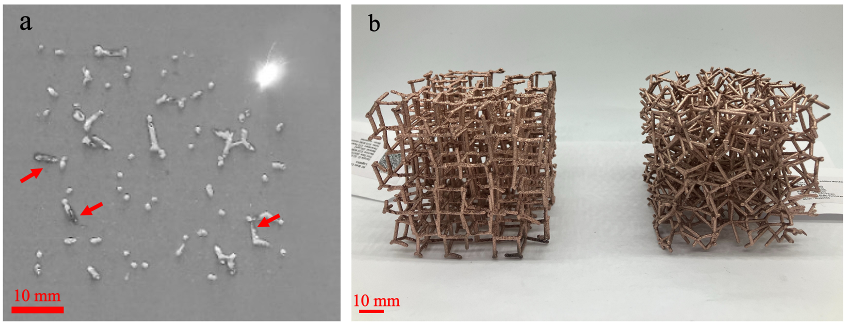

Figure 3: *(a)* The disordered melted pattern of a layer with arrows indicating overheating and oxidation *(b)* MDM geometries fabricated with LPBF

.

shown in Figure 4a. The printed cylinders were compared with their nominal STL file, resulting in cloud-to-mesh signed distance [100, 101] heat maps, shown in Figure 4b. The heat maps reveal a decrease in geometric accuracy for 1.0 mm to 3.0 mm diameter cylinders printed at angles less than 30°, regardless of cylinder diameter. At low angles, large deviations in geometry are observed on the downfacing surfaces of the cylinders, where the laser is printing directly onto the powder bed. This is represented by the blue (negative) or red (positive) dimension scale, where the cylinders' surfaces are significantly distorted or swept away during recoating, until stable enough to build upon.

Figure 4c shows the geometric deviation of the cylinders at 10°, 30°, 60° and 90°, as measured along the distance from the base. The measured values in Figure 4c reveal an effect of diameter and angle on the geometric accuracy of the cylinders. At 90°, negligible deviation occurs for both the 260 W and 220 W energy conditions. For example, at 90° the 260 W, 3.0 mm diameter cylinders have an average geometric deviation of 0.027 ± 0.016 mm, and the 220 W, 3.0 mm diameter cylinders have an average deviation of 0.044 ± 0.019 mm. The larger deviation in the 220 W specimens can be attributed to powder agglomerations on the surface, not seen in the 260 W cylinders, for this specific sample set. The deviation slowly increases as the print angle decreases. However, at 10°, significant geometric inaccuracy is measured in the unsupported cylinders of diameters of 3.0 and 2.0 mm, with the 1.0 mm cylinders showing reduced geometric deviations. For example at 10°, the 260 W, 3.0 mm cylinders have an average deviation of 0.21 ± 0.15 mm and the 220 W, 3.0 mm cylinders have an average deviation of 0.070 ± 0.066 mm. A decline in quality with increasing overhang angle is often reported in LPBF literature, due to the difference in thermal conductivity between the point contacts of powder particles in the bed, compared with printing on a solid substrate of the same composition. As the overhang area increases, more of the geometry prints directly onto the powder bed in the first several layers of a given feature, leading to heat build-up and infiltration of the melt pool into the bed. This has been shown to cause geometric inaccuracy, dross formation, or failure [73, 72, 74, 102, 103, 104].

From the results in Figure 4, it is apparent that both the standard and reduced melt parameters produce similar geometric deviation for the cylinders. However for the remainder of the study, both the cylinders and MDM geometries were fabricated using the reduced melt parameters. The reduced parameters developed in this work were found to be on the lowest end of allowable energy density for the GRCop-42 process window that produced near full density cylinders, while minimizing the thermal stress experienced in the part as compared to the 260 W melt parameters. Based on the these results, select sets of unsupported and supported 2.0 mm diameter cylinders were printed at 10° to focus on the difficult, low-angle beams. The downskin parameters of these cylinders were varied to determine the effect of heat input on geometric accuracy. These results are compiled in Figure 5 and Table 2. The geometric deviation of the cylinders is also plotted as a function of the distance from the base, shown in Figure 5b and 5d.

Figure 5a shows the geometric deviation heat maps for the unsupported 2.0 mm cylinders printed with reduced 220 W melt parameters and varied downskins. As the power in the downskin increases, the geometric deviation also increases especially on the downfacing surfaces. This can also be seen in the deviation graphs in Figure 5b and the average geometric and standard deviations calculated in Table 2. For example, the 96 W downskin resulted in an average geometric deviation of 0.092 ± 0.075 mm, while the 126 W downskin resulted in an average geometric deviation of 0.15 ± 0.11 mm. Figure 5c and 5d show the geometric deviation heat maps and corresponding graphs for 2.0 mm cylinders printed with the custom support design and parameters. The supported cylinders were fabricated with the reduced 220 W melt parameters and 96 W downskin, as these parameters produced the

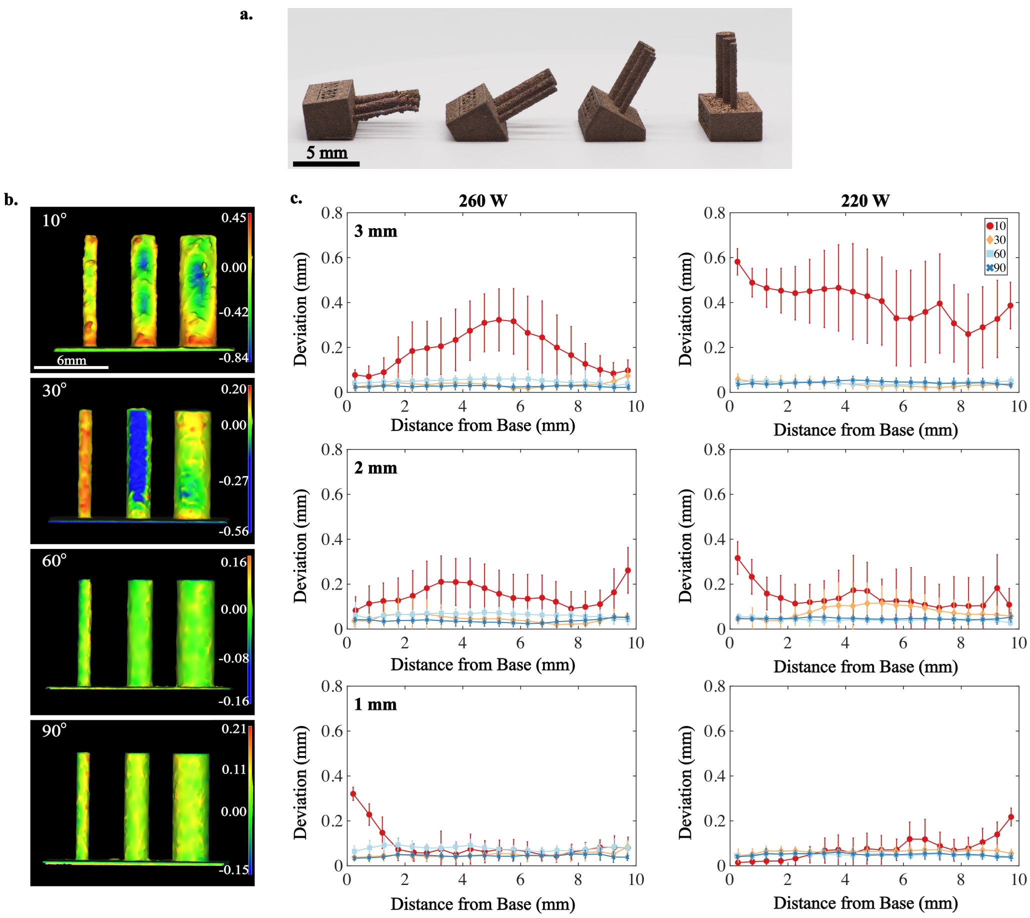

Figure 4: Geometric accuracy of thin wall cylinders *(a)* Unsupported cylinders ranging from 10° to 90° , *(b)* Geometric deviation heat maps (dimensions in mm) of the downfacing regions of unsupported cylinders printed with 220 W, *(c)* Geometric deviation with respect to distance of the cylinder from the base for varied cylinder diameter, overhang angle, and power using 'Original' downskin parameters in Table 1. Error bars are calculated as standard deviations.

best geometric accuracy for the 2.0 mm unsupported cylinders printed at 10°. In comparing the average geometric deviation and the standard deviation of the unsupported cylinders and the supported cylinders, it is clear that the addition of supports has a significant impact on the geometric deviation. For example, the 96 W unsupported cylinder has an average geometric deviation of 0.092 ± 0.075 mm, whereas the 96 W cylinder with a support 1 strategy has an average geometric deviation of 0.051 ± 0.049 mm.

As described in the methods section, a total of 10 unique support designs were tested on a quarter of a hyperuniform MDM to observe how the support parameters influenced geometric integrity and ease of support removal. From those 10 support designs, a total of 3 were downselected upon that criteria, and are listed in Figure 2b. The effectiveness of each support design was then quantified on the standalone cylinders, as seen in Figure 5c and 5d and Table 2. The results show a negligible difference in the average and standard geometric deviation of the supported cylinders with support strategies 1 and 3. However the results differ for support strategy 2, with an average geometric deviation of 0.068 ± 0.079 mm. It can be observed from the heat map of strategy 2 in Figure 5c, that not only was the downfacing side of the cylinder thermally unstable, indicated by the negative dimension in blue, but the surface also contained a significant amount of agglomerated powder particles. This is due to the combination of support parameters used. For example, when comparing strategy 2 with strategy 1, strategy 2 has a larger anchor distance leading to less anchor points, thereby decreasing the total amount of support and contributing to the increase in average geometric deviation. In comparing strategy 2 with strategy 3, they have the same anchor distance, however strategy 3 has more surface in contact with the connecting beam, indicated by "width at end" in Table 1. With less support material in contact with the connecting beam, strategy 2 results in larger deviations than strategy 3, likely due to insufficient heat removal.

The downksin results in conjunction with the initial unsupported cylinders in Figure 4 demonstrate that there exists a fine thermal balance in the downskin parameters for unsupported, low-angle connecting beams. The original downskins used for both the standard and reduced melt parameters had insufficient energy in the first few layers of the print. When the melt parameters subsequently melted in the layers above, the downskin likely could not support the thermal stress, resulting in larger geometric inaccuracies on the downfacing surface compared to the cylinders with higher energy downskins. However when the downskin energy was too high, the liquid melt pool infiltrated the powder bed [71, 69], increasing the geometric deviation due to powder agglomerations on the surface or loss of geometry. Additionally, the standalone cylinder results emphasize that the addition of supports plays a more influential role in improving geometric integrity of overhanging geometries as compared to tuning the downskin parameters, since the supports act as a heat sink.

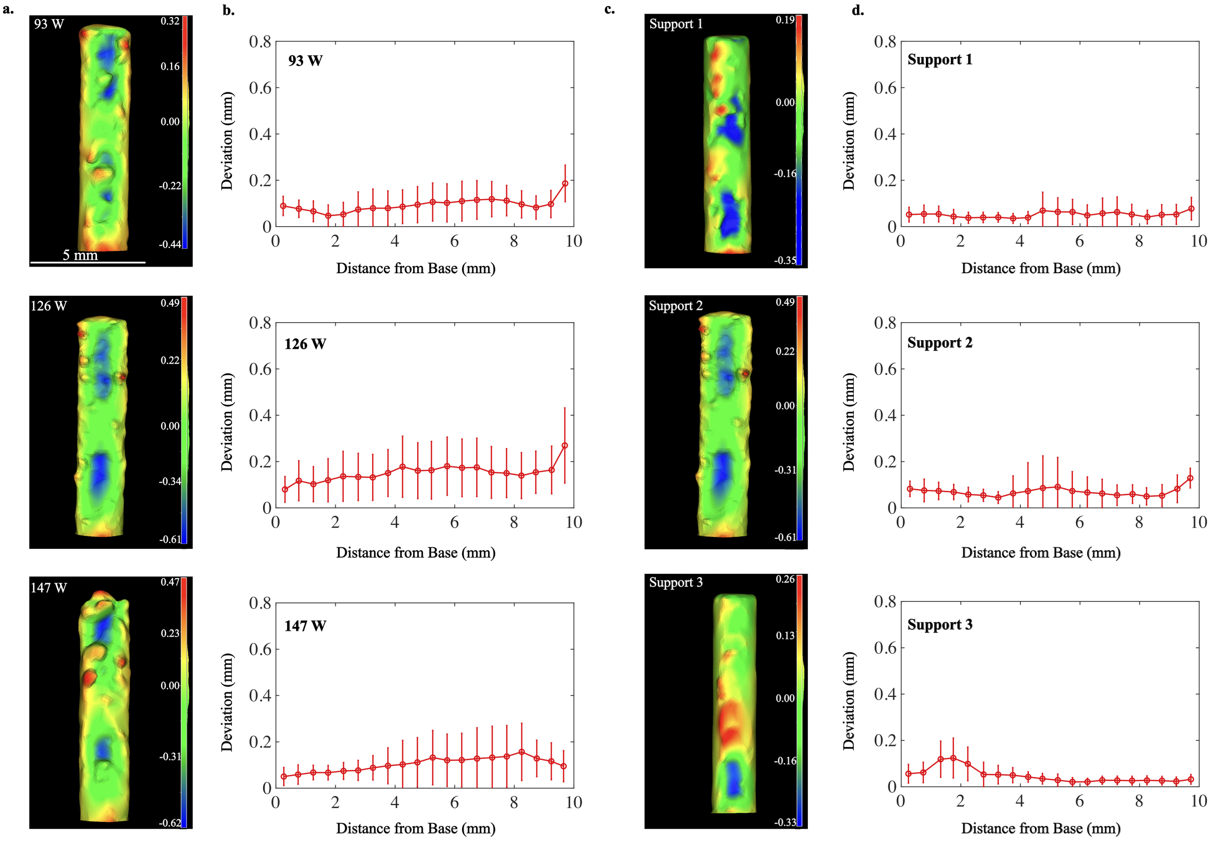

Figure 5: Effect of downskin parameters and supports on geometric deviation of thin wall cylinders. *(a)* Deviation (dimensions in mm) heat maps of the downfacing surfaces of unsupported, 2.0 mm cylinders printed with 220 W melt parameters at an angle of 10°, and varied downskin parameters *(b)* Geometric deviation with respect to distance from the print base for 220 W , 2.0 mm diameter cylinders, with varied downskin, *(c)* Deviation heat maps of the downfacing surfaces of supported, 2.0 mm cylinders printed with a 96 W downskin and varied support strategies, *(d)* Geometric deviation with respect to distance from the print base for 2.0 mm cylinders and varied support strategies. Error bars are calculated as standard deviation.

Print Condition	Avg	STD
96 W	0.092	0.075
126 W	0.15	0.11
147 W	0.11	0.10
Support 1	0.051	0.049
Support 2	0.068	0.079
Support 3	0.046	0.050

Table 2: Average geometric deviation and standard deviation for 2.0 mm cylinders manufactured with varying downskin and support parameters at 10°. All results in mm.

Previous studies have reported similar results on the effects of process parameters and overhang angles on thin walls and overhanging geometric features. Fox et al. [71] fabricated parallelepipeds with overhang angles of 30°, 45°, 60°, and 75°, with varied parameters. Their results showed higher energy parameters induced more thermal stress in the part, and that surface roughness increased with increasing overhang angle. Wang et al. [105] found that for overhanging geometries, dross formation, and warping effects were caused by higher input energy [69].

Wu et al. [73] fabricated thin walls of varying thickness (100 to 900 microns) and overhang angles (30°, 45°, and 60°) to determine fabrication limits for thin wall structures in LPBF. They found that minimum wall thicknesses can be successfully built using lower energy parameters. Furthermore, Xie et al. [99] reported that wall thickness deviation increased with increasing power.

Other studies detailed the significant influence of overhang angle on the surface quality and dimensional accuracy of LPBF parts. Zhao et al. [106] reported that the overhang angle itself had the largest impact on dimensional accuracy and surface quality for thin wall struts, with the downfacing surface having the greatest surface roughness. McGregor et al. [52] evaluated downfacing surfaces of 1.0 mm thick struts in a lattice geometry, and observed poor geometric fidelity of downfacing surfaces with an overhang angle of 15°or less. Shange et al. [72] fabricated parallelepipeds with overhang angles ranging from 25° to 90° at 5° increments. They observed large amounts of powder agglomeration on the downfacing surfaces at low angles, mainly fabricated below 45°.

A Gaussian, moving heat source, thermal model was used to gain insight into how melt pools form at varying laser powers and thermal conductivities. The ambient thermal conductivity (k) for GRCop-42 is typically 330 W/m·K. However, the thermal conductivity of the powder bed may be as low as 0.17 W/m·K, due to point contacts of the powder [107, 108, 109, 102, 103, 104, 110, 111]. This difference in thermal conductivity is likely a major contributor to the observed failure and geometric deviation of low-angle connecting beams and cylinders printed in this study. Figure 6 shows the simulated melt pool temperatures for varied processing conditions. Estimated k values of 33 and 330 W/m·K [109] were used to represent the thermal conductivity extremes of the LPBF process, printing connecting beams or cylinders between 90° (vertical) and 10° (horizontal), respectively. Figure 6 shows the 220 W melt and 96 W downskin parameters with estimated temperatures approaching 3300 K and 1500 K for the 90°cylinders, respectively. Temperatures at decreasing angles rise sharply at 30°and below, where the melt temperatures approach 6000 K while the downskin exceeds 3000 K.

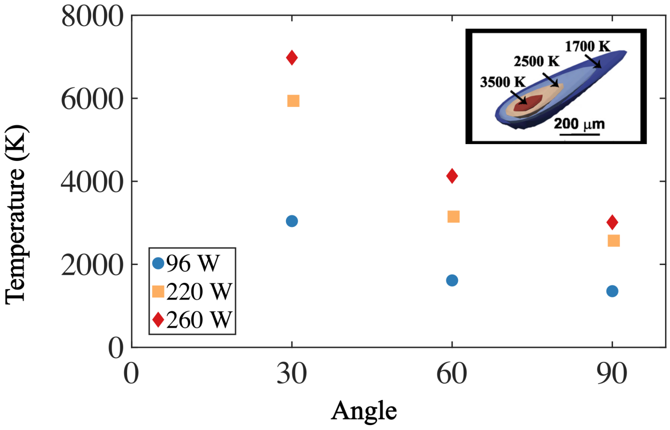

Figure 6: Simulated melt pool maximum temperature with variations in thermal conductivity and laser power. The inset in the top right shows an example of a simulated melt pool with temperature contours.

These estimated temperatures imply there is a fine thermal balance associated with printing supportless, low-angle, connecting beams. If the downskin energy is too low, the relatively cool, small melt pools may not overlap sufficiently within the 70 micron hatch, leaving them prone to significant lack of fusion defects and failure upon subsequent melt parameters. If the downfacing surfaces become too hot, they may oxidize or the liquid may infiltrate into the bed, potentially causing significant geometric deviation or connecting beam failure, upon subsequent melting. For simple cylinders with a constant overhang angle, optimization of the downskin is more straightforward. However, the aperiodic beam angles of the MDM geometry make implementing a single downskin parameter challenging, since the angles are changing layer to layer. Therefore, heat input and parameters may need to be tuned for each 2D layer as connecting beam angle, beam size, and beam density change with Z-location in an MDM geometry.

A final print of the two MDMs (Hyperuniform and Granular) was performed, utilizing lessons learned, to try and produce more accurate geometries compared with its nominal STL file. XRCT results for the final supported 65 mm footprint MDMs are compared with unsupported MDMs, as shown in Figure 7. The geometries were fabricated using the reduced melt and down selected downskin parameters, see Table 1. The supports were generated using strategy 3, described in Figure 2b, and placed throughout the geometry at angles below 30° to help dissipate heat in the beams and improve large overhanging connecting beams.

Figure 7a shows the geometric deviation heat maps for each of the unsupported and supported MDMs. The unsupported hyperuniform (UH) MDM behaved as expected, with connecting beams below 30°showing large geometric deviation up to 7.53 mm, indicated by the red dimension on the heat map. The corresponding probability distribution of geometric deviation for the UH MDM can be seen in Figure 7b, showing an overall average geometric deviation of 0.22 ± 0.62 mm. In contrast, the supported hyperuniform (SH) MDM counterpart reduced the geometric deviation for the low-angle connecting beams, as is notably observed by the decreased red dimension present in the heat map in Figure 7a. Additionally, the probability distribution shows improvement in the average geometric deviation with a result of 0.19 ± 0.43 mm. The granular MDMs show a similar trend, with the unsupported granular (UG) MDM having an average geometric deviation of 0.18 ± 0.54 mm, compared to the supported granular (SG) MDM with an average geometric deviation of 0.069 ± 0.39 mm. It is important to note that the inherent complexity of the geometry, including total number of connecting beams and proportion of connecting beams with large overhangs play a significant role in the outcome of these results. The granular geometries contain not only less total number of connecting beams, but also considerably less overhangs than that of the hyperuniform MDM. Therefore the geometric accuracy of the granular geometry, even unsupported, is greater than that of the hyperuniform MDMs.

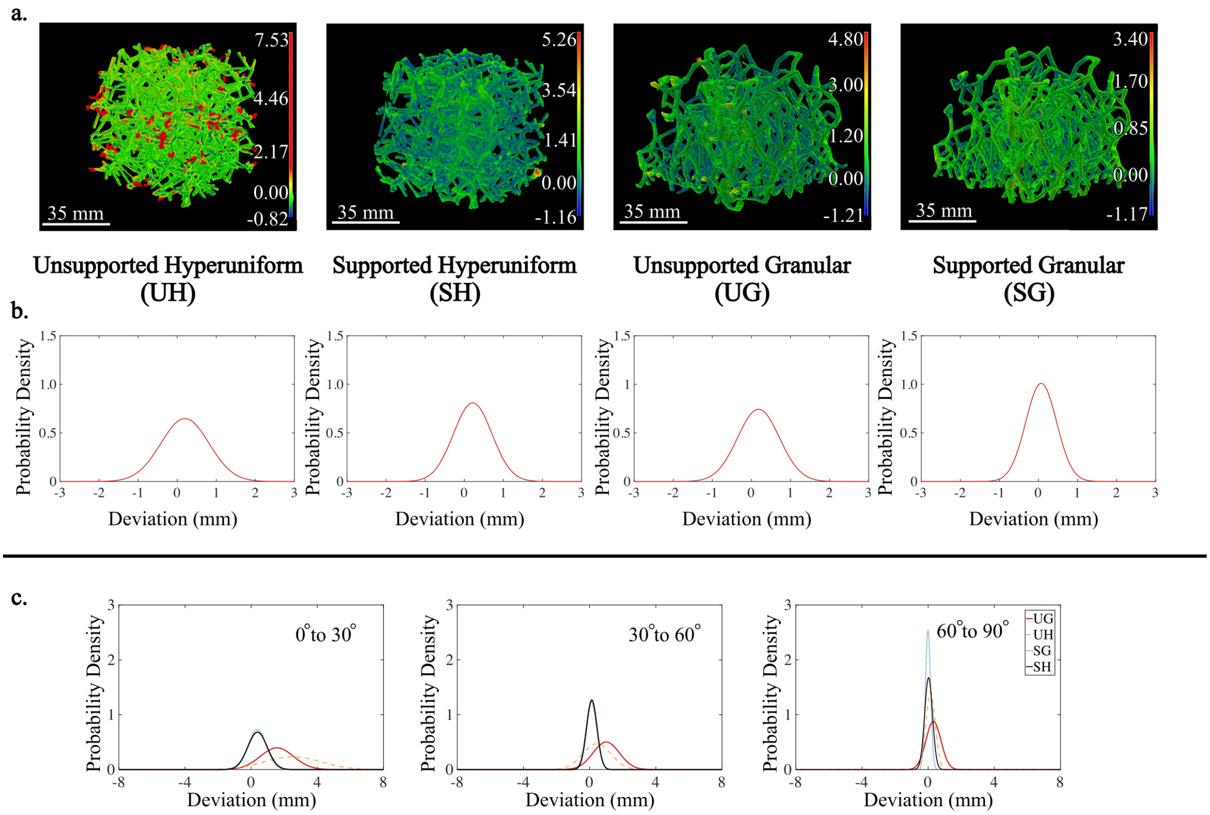

Figure 7: Characterization of unsupported and supported geometries by Computed Tomography. *(a)* Geometric deviation heat maps of MDM geometries: Unsupported Hyperuniform (UH), Supported Hyperuniform (SH), Unsupported Granular (UG), Supported Granular (SG), *(b)* Normal probability distribution of MDM geometric deviation with and without supports, *(c)* Normal probability distribution of geometric deviation for ranges of connecting beam angles in the MDM geometries.

Individual connecting beams from angle groupings of 0° to 30°, 30° to 60°, and 60° to 90° were analyzed, and their normal probability distributions for geometric deviation shown in Figure 7c and written in Table 3. The greatest deviations are found on the downfacing surfaces of connecting beams in the 10° to 30° grouping. Similar observations are shown for the unsupported standalone cylinders in Figures 4 and 5. However, the supported MDM geometries still show improvement in this low angle range, with an average deviation across several measured beams of 0.38 ± 0.59 mm in the hyperuniform MDM and 0.37 ± 0.59 mm in the granular MDM. In comparison, the originally printed unsupported geometries have an average deviation of 2.51 ± 1.71 mm in the hyperuniform MDM and 1.56 ± 1.01 mm in the granular MDM. As discussed in the previous results, geometric inaccuracy of downfacing surfaces at these low angles is due to powder agglomeration from heat build-up and melt pool infiltration into the surrounding powder. Many of the connecting beams with large overhang angles also display significant deviations due to thermal warping from excess heat during printing. These issues can be most effectively mitigated through the use of supports and lower energy melt and downskin conditions, as shown in

Figures 4 and 5 and further confirmed in Figure 7.

	0°-30°	**30°-60°**	**60°-90°**
UH	2.51 ± 1.71	0.43 ± 0.85	0.15 ± 0.28
SH	0.38 ± 0.59	0.13 ± 0.31	0.027 ± 0.24
UG	1.56 ± 1.01	1.00 ± 0.79	0.32 ± 0.45
SG	0.37 ± 0.55	0.11 ± 0.33	0.01 ± 0.16

Table 3: Average geometric deviation and standard deviation for 1.5 mm connecting beams in unsupported and supported MDM hyperuniform and granular geometries. All results in mm.

As the print angle increases, the average geometric deviation improves with the supported geometries showing the lowest deviation. In the angle range of 30° to 60°, the supported connecting beams have an average deviation of 0.13 ± 0.31 mm in the hyperuniform MDM and 0.11 ± 0.33 mm in the granular MDM, compared to the unsupported geometries with an average deviation of 0.43 ± 0.85 mm in the hyperuniform MDM and 1.00 ± 0.79 mm in the granular MDM. The lowest geometric deviation is seen in the 60° to 90° range, with the connecting beams in supported geometry having an average deviation of 0.027 ± 0.24 mm in the hyperuniform MDM, and 0.01 ± 0.16 mm in the granular MDM. In contrast, the unsupported geometries have larger deviations even at increased angles with an average deviation of 0.15 ± 0.28 mm for the hyperuniform MDM and 0.32 ± 0.45 mm for the granular MDM. The geometric deviation is less for all unsupported and supported conditions in this angle range, as the laser is remelting on a mostly solid area, thereby improving heat dissipation in the connecting beams and reducing thermal warping and failure.

While the overall probability distribution curves for both MDM geometries indicate small improvements in the total geometric accuracy with the addition of supports, distribution curves for each angle range show the significant improvements made for the overhanging connecting beams. Not only did the average geometric accuracy of the supported counterparts improve, but the variability for the connecting beams noticeably decreased. As the angle increased, the accuracy improved as expected, however it should be noted that even for the self supporting angle range of 60° to 90° the unsupported MDM geometries were less accurate than their supported counterparts. This is most likely due to the added heat transfer supports contribute for the overall thermal balance of the bed, which when lacking cause greater geometric deviations in the geometry. In total, these results emphasize the critical roles that downskin and supports have on improving the quality and survival of overhanging features to successfully fabricate geometrically accurate metallic disordered metamaterials.

5. Conclusions

Metallic disordered metamaterial (MDM) geometries were successfully fabricated using GRCop-42 on an EOS M290 LPBF system. This was achieved through an iterative process of parameter and support development that began as STL files generated using a published 3D bidisperse granular system and a uniformly randomized lattice (URL), hyperuniform point cloud. These geometries presented multiple manufacturing challenges: aperiodic beam angles and overhangs, difficult-to-access support removal, and gradient beam density in the case of the granular geometry.

To address some of these challenges, we performed cylinder prints to fine-tune the melt, downskin and support strategies. It was found that a 220 W melt parameter, with a 96 W downskin parameter, and supports resulted in the lowest geometric deviation for 2.0 mm cylinders at 10°of 0.046 ± 0.050 mm. Supported and unsupported granular and hyperuniform MDM geometries were fabricated for a final comparison, with 1.5 mm diameter connecting beams, 220 W melt parameters, and a strategically designed supports. The geometric accuracy of both the granular and hyperuniform MDM's were improved, upon the addition of supports with a final average geometric deviation of 0.069 ± 0.39 mm and 0.22 ± 0.62 mm, respectively. Future work will involve more intensive model-guided predictions to fine-tune melt and downskin strategies to successfully print low-angle connecting beams with a limited number of supports.

Acknowledgments:. This work is supported by the collaborative NSF DMREF grant number CMMI-2323341. Additionally K.L. and R.C.H. acknowledge support from NSF DMREF grant number CMMI-2323344 and K.N and C.E.M. from CMMI-2323342. This work was aalso greatly supported by North Carolina State University's Center for Additive Manufacturing and Logistics. This work was performed in part at the Analytical Instrumentation Facility (AIF) at North Carolina State University, which is supported by the State of North Carolina and the National Science Foundation (award number ECCS-2025064). The AIF is a member of the North Carolina

Research Triangle Nanotechnology Network (RTNN), a site in the National Nanotechnology Coordinated Infrastructure (NNCI). We are grateful to former group members Michael Miller and Estelle Berthier, who generated the STL file of the disordered metamaterial under support from the James S. McDonnell Foundation. The authors would like to thank J. Raj for assistance in the generation of network structures.

Data is available on request.

References

[1] A. Shih, M. Casiulis, S. Martiniani, Fast generation of spectrally shaped disorder, Physical Review E 110 (2024) 034122. URL: `https://link.aps.org/doi/10.1103/PhysRevE.110.034122`. doi:`10.1103/PhysRevE.110.034122`.

[2] M. Sahimi, Heterogeneous Materials I, volume 22 of *Interdisciplinary Applied Mathematics*, Springer-Verlag, New York, 2003. URL: `http://link.springer.com/10.1007/b97507`. doi:`10.1007/b97507`.

[3] J. Mueller, K. H. Matlack, K. Shea, C. Daraio, Energy Absorption Properties of Periodic and Stochastic 3D Lattice Materials, Advanced Theory and Simulations 2 (2019) 1900081. doi:`10.1002/adts.201900081`.

[4] L. Bao, T. J. Cui, Tunable, reconfigurable, and programmable metamaterials, Microwave and Optical Technology Letters 62 (2020) 9–32. URL: `https://onlinelibrary.wiley.com/doi/10.1002/mop.32164`. doi:`10.1002/mop.32164`.

[5] L. Dong, J. Wang, D. Wang, Modeling and design of three-dimensional voxel printed lattice metamaterials, Additive Manufacturing 69 (2023) 103532. URL: `https://linkinghub.elsevier.com/retrieve/pii/S2214860423001458`. doi:`10.1016/j.addma.2023.103532`.

[6] Z. Jia, F. Liu, X. Jiang, L. Wang, Engineering lattice metamaterials for extreme property, programmability, and multifunctionality, Journal of Applied Physics 127 (2020) 150901. URL: `https://pubs.aip.org/jap/article/127/15/150901/156852/Engineering-lattice-metamaterials-for-extreme`. doi:`10.1063/5.0004724`.

[7] J. Bauer, L. R. Meza, T. A. Schaedler, R. Schwaiger, X. Zheng, L. Valdevit, Nanolattices: An Emerging Class of Mechanical Metamaterials, Advanced Materials 29 (2017) 1701850. URL: `https://onlinelibrary.wiley.com/doi/10.1002/adma.201701850`. doi:`10.1002/adma.201701850`.

[8] M. Florescu, S. Torquato, P. J. Steinhardt, Designer disordered materials with large, complete photonic band gaps, Proceedings of the National Academy of Sciences 106 (2009) 20658–20663. URL: `https://pnas.org/doi/full/10.1073/pnas.0907744106`. doi:`10.1073/pnas.0907744106`.

[9] S. Torquato, D. Chen, Multifunctional hyperuniform cellular networks: optimality, anisotropy and disorder, Multifunctional Materials 1 (2018) 015001. URL: `https://iopscience.iop.org/article/10.1088/2399-7532/aaca91`. doi:`10.1088/2399-7532/aaca91`.

[10] F. Bigourdan, R. Pierrat, R. Carminati, Enhanced absorption of waves in stealth hyperuniform disordered media, Optics Express 27 (2019) 8666–8682. doi:`10.1364/OE.27.008666`.

[11] Y. Huang, K. E. Daniels, Friction and pressure-dependence of force chain communities in granular materials, Granular Matter 18 (2016) 85. URL: `http://link.springer.com/10.1007/s10035-016-0681-6`. doi:`10.1007/s10035-016-0681-6`.

[12] A. Hemmerle, M. Schrter, L. Goehring, A cohesive granular material with tunable elasticity, Scientific Reports 6 (2016) 35650. URL: `https://www.nature.com/articles/srep35650`. doi:`10.1038/srep35650`.

[13] S. Torquato, F. H. Stillinger, Local density fluctuations, hyperuniformity, and order metrics, Physical Review E 68 (2003) 041113. doi:`10.1103/PhysRevE.68.041113`.

[14] S. Torquato, Hyperuniform states of matter, Physics Reports 745 (2018) 1–95. doi:`10.1016/j.physrep.2018.03.001`.

[15] P. Debye, H. R. Anderson, Jr., H. Brumberger, Scattering by an Inhomogeneous Solid. II. The Correlation Function and Its Application, Journal of Applied Physics 28 (1957) 679–683. URL: `https://doi.org/10.1063/1.1722830`. doi:`10.1063/1.1722830`.

[16] Y. Jiao, T. Lau, H. Hatzikirou, M. Meyer-Hermann, Joseph C. Corbo, S. Torquato, Avian photoreceptor patterns represent a disordered hyperuniform solution to a multiscale packing problem, Physical Review E 89 (2014) 022721. URL: `https://link.aps.org/doi/10.1103/PhysRevE.89.022721`. doi:`10.1103/PhysRevE.89.022721`.

[17] Z. Ge, The hidden order of Turing patterns in arid and semiarid vegetation ecosystems, Proceedings of the National Academy of Sciences 120 (2023) e2306514120. URL: `https://www.pnas.org/doi/10.1073/pnas.2306514120`. doi:`10.1073/pnas.2306514120`, publisher: Proceedings of the National Academy of Sciences.

[18] Y. Liu, D. Chen, Y. Jiao, J. Tian, Universal Hyperuniform Organization of Cellular Structures in Leaf Vein Networks, Technical Report arXiv:2311.09551, arXiv, 2023. URL: `http://arxiv.org/abs/2311.09551`, arXiv:2311.09551 [cond-mat] type: article.

[19] P. J. E. P. J. E. Peebles, Principles of physical cosmology, Princeton, N.J. : Princeton University Press, 1993. URL: `http://archive.org/details/principlesofphys00pjep`.

[20] O. H. Philcox, S. Torquato, Disordered Heterogeneous Universe: Galaxy Distribution and Clustering across Length Scales, Physical Review X 13 (2023) 011038. URL: `https://link.aps.org/doi/10.1103/PhysRevX.13.011038`. doi:`10.1103/PhysRevX.13.011038`, publisher: American Physical Society.

[21] A. Donev, F. H. Stillinger, S. Torquato, Unexpected Density Fluctuations in Jammed Disordered Sphere Packings, Physical Review Letters 95 (2005) 090604. URL: `https://link.aps.org/doi/10.1103/PhysRevLett.95.090604`. doi:`10.1103/PhysRevLett.95.090604`, publisher: American Physical Society.

[22] J. H. Weijs, R. Jeanneret, R. Dreyfus, D. Bartolo, Emergent Hyperuniformity in Periodically Driven Emulsions, Physical Review Letters 115 (2015) 108301. doi:`10.1103/PhysRevLett.115.108301`.

[23] S. Wilken, R. E. Guerra, D. J. Pine, P. M. Chaikin, Hyperuniform Structures Formed by Shearing Colloidal Suspensions, Physical Review Letters 125 (2020) 148001. doi:`10.1103/PhysRevLett.125.148001`.

[24] S. Wilken, R. E. Guerra, D. Levine, P. M. Chaikin, Random Close Packing as a Dynamical Phase Transition, Physical Review Letters 127 (2021) 038002. doi:`10.1103/PhysRevLett.127.038002`.

[25] J. R. Dale, J. D. Sartor, R. C. Dennis, E. I. Corwin, Hyperuniform jammed sphere packings have anomalous material properties, Physical Review E 106 (2022) 024903. doi:`10.1103/PhysRevE.106.024903`.

[26] C. E. Maher, S. Torquato, Hyperuniformity scaling of maximally random jammed packings of two-dimensional binary disks, 2024. URL: `http://arxiv.org/abs/2412.10883`. doi:`10.48550/arXiv.2412.10883`, arXiv:2412.10883.

[27] Y. Jiao, S. Torquato, Maximally random jammed packings of Platonic solids: Hyperuniform long-range correlations and isostaticity, Physical Review E 84 (2011) 041309. URL: https://link.aps.org/doi/10.1103/PhysRevE.84.041309. doi:10.1103/PhysRevE.84.041309.

[28] G. Cinacchi, S. Torquato, Hard convex lens-shaped particles: Characterization of dense disordered packings, Physical Review E 100 (2019) 062902. URL: https://link.aps.org/doi/10.1103/PhysRevE.100.062902. doi:10.1103/PhysRevE.100.062902, publisher: American Physical Society.

[29] C. E. Maher, F. H. Stillinger, S. Torquato, Characterization of void space, large-scale structure, and transport properties of maximally random jammed packings of superballs, Physical Review Materials 6 (2022) 025603. URL: https://link.aps.org/doi/10.1103/PhysRevMaterials.6.025603. doi:10.1103/PhysRevMaterials.6.025603.

[30] J. Kim, S. Torquato, New tessellation-based procedure to design perfectly hyperuniform disordered dispersions for materials discovery, Acta Materialia 168 (2019) 143–151. URL: https://www.sciencedirect.com/science/article/pii/S1359645419300412. doi:10.1016/j.actamat.2019.01.026.

[31] D. Chen, S. Torquato, Designing disordered hyperuniform two-phase materials with novel physical properties, Acta Materialia 142 (2018) 152–161. doi:10.1016/j.actamat.2017.09.053.

[32] E. Chertkov, R. A. DiStasio, G. Zhang, R. Car, S. Torquato, Inverse design of disordered stealthy hyperuniform spin chains, Physical Review B 93 (2016) 064201. URL: https://link.aps.org/doi/10.1103/PhysRevB.93.064201. doi:10.1103/PhysRevB.93.064201.

[33] R. A. DiStasio, G. Zhang, F. H. Stillinger, S. Torquato, Rational design of stealthy hyperuniform two-phase media with tunable order, Physical Review E 97 (2018) 023311. URL: https://link.aps.org/doi/10.1103/PhysRevE.97.023311. doi:10.1103/PhysRevE.97.023311.

[34] S. Torquato, Y. Jiao, Robust algorithm to generate a diverse class of dense disordered and ordered sphere packings via linear programming, Physical Review E 82 (2010) 061302. doi:10.1103/PhysRevE.82.061302.

[35] S. Torquato, Extraordinary disordered hyperuniform multifunctional composites, Journal of Composite Materials 56 (2022) 3635–3649. URL: http://journals.sagepub.com/doi/10.1177/00219983221116432. doi:10.1177/00219983221116432.

[36] W. Man, M. Florescu, E. P. Williamson, Y. He, S. R. Hashemizad, B. Y. C. Leung, D. R. Liner, S. Torquato, P. M. Chaikin, P. J. Steinhardt, Isotropic band gaps and freeform waveguides observed in hyperuniform disordered photonic solids, Proceedings of the National Academy of Sciences 110 (2013) 15886–15891. doi:10.1073/pnas.1307879110.

[37] D. Chen, Y. Zheng, L. Liu, G. Zhang, M. Chen, Y. Jiao, H. Zhuang, StoneWales defects preserve hyperuniformity in amorphous two-dimensional networks, Proceedings of the National Academy of Sciences 118 (2021). doi:10.1073/pnas.2016862118.

[38] D. Chen, Y. Zheng, Y. Jiao, Topological defects, inherent structures, and hyperuniformity, Physical Review B 104 (2021) 174101. doi:10.1103/PhysRevB.104.174101.

[39] N. Muller, J. Haberko, C. Marichy, F. Scheffold, Silicon Hyperuniform Disordered Photonic Materials with a Pronounced Gap in the Shortwave Infrared, Advanced Optical Materials 2 (2014) 115–119. doi:10.1002/adom.201300415.

[40] R. M. Besana, F. Elas, J. Puig, J. A. Snchez, G. Nieva, A. B. Kolton, Y. Fasano, Finite-size effects in hyperuniform vortex matter, 2024. URL: http://arxiv.org/abs/2403.05915, arXiv:2403.05915 [cond-mat].

[41] Y. Xu, S. Chen, P.-E. Chen, W. Xu, Y. Jiao, Microstructure and mechanical properties of hyperuniform heterogeneous materials, Physical Review E 96 (2017) 043301. URL: https://link.aps.org/doi/10.1103/PhysRevE.96.043301. doi:10.1103/PhysRevE.96.043301.

[42] E. Chron, J.-P. Groby, V. Pagneux, S. Flix, V. Romero-Garca, Experimental characterization of rigid-scatterer hyperuniform distributions for audible acoustics, Physical Review B 106 (2022) 064206. URL: https://link.aps.org/doi/10.1103/PhysRevB.106.064206. doi:10.1103/PhysRevB.106.064206.

[43] W. J. Sames, F. A. List, S. Pannala, R. R. Dehoff, S. S. Babu, The metallurgy and processing science of metal additive manufacturing, International Materials Reviews 61 (2016) 315–360. doi:10.1080/09506608.2015.1116649.

[44] T. DebRoy, H. L. Wei, J. S. Zuback, T. Mukherjee, J. W. Elmer, J. O. Milewski, A. M. Beese, A. Wilson-Heid, A. De, W. Zhang, Additive manufacturing of metallic components Process, structure and properties, Progress in Materials Science 92 (2018) 112–224. doi:10.1016/j.pmatsci.2017.10.001.

[45] S. A. Tofail, E. P. Koumoulos, A. Bandyopadhyay, S. Bose, L. ODonoghue, C. Charitidis, Additive manufacturing: scientific and technological challenges, market uptake and opportunities, Materials Today 21 (2018) 22–37. URL: https://linkinghub.elsevier.com/retrieve/pii/S1369702117301773. doi:10.1016/j.mattod.2017.07.001.

[46] D. R. Eyers, A. T. Potter, J. Gosling, M. M. Naim, The flexibility of industrial additive manufacturing systems, International Journal of Operations & Production Management 38 (2018) 2313–2343. URL: https://www.emerald.com/insight/content/doi/10.1108/IJOPM-04-2016-0200/full/html. doi:10.1108/IJOPM-04-2016-0200.

[47] L. Siedentop, G. Lui, G. Maret, P. M. Chaikin, P. J. Steinhardt, S. Torquato, P. Keim, M. Florescu, Stealthy and hyperuniform isotropic photonic band gap structure in 3D, PNAS Nexus 3 (2024) pgae383. URL: https://academic.oup.com/pnasnexus/article/doi/10.1093/pnasnexus/pgae383/7750454. doi:10.1093/pnasnexus/pgae383.

[48] M. Sniechowski, J. Kaminski, S. Wronski, Heterogeneous materials based on aperiodic structures for bone tissue substitutes, VI International Conference on Computational Bioengineering ICCB (2015).

[49] A. Wit, S. Wronski, J. Tarasiuk, Simulation and optimization of porous bone-like microstructures with specific mechanical properties, Acta Polytechnica CTU Proceedings 25 (2019) 89–92. URL: https://ojs.cvut.cz/ojs/index.php/APP/article/view/6035. doi:10.14311/APP.2019.25.0089.

[50] A. Gromann, J. Felger, T. Frlich, J. Gosmann, C. Mittelstedt, Melt pool controlled laser powder bed fusion for customised low-density lattice structures, Materials & Design 181 (2019) 108054. URL: https://linkinghub.elsevier.com/retrieve/pii/S0264127519304927. doi:10.1016/j.matdes.2019.108054.

[51] X. Wang, L. Zhang, B. Song, Z. Zhang, J. Zhang, J. Fan, S. Wei, Q. Han, Y. Shi, Tunable mechanical performance of additively manufactured plate lattice metamaterials with half-open-cell topology, Composite Structures 300 (2022) 116172. URL: https://linkinghub.elsevier.com/retrieve/pii/S0263822322009047. doi:10.1016/j.compstruct.2022.116172.

[52] M. McGregor, S. Patel, K. Zhang, A. Yu, M. Vlasea, S. McLachlin, A manufacturability evaluation of complex architectures by laser powder bed fusion additive manufacturing, Journal of Manufacturing Science and Engineering 146 (2024) 061007. doi:10.1115/1.4065315.

[53] J. Yang, X. Jin, H. Gao, D. Zhang, H. Chen, S. Zhang, X. Li, Additive manufacturing of trabecular tantalum scaffolds by laser powder bed fusion: Mechanical property evaluation and porous structure characterization, Materials Characterization 170 (2020) 110694. URL: https://linkinghub.elsevier.com/retrieve/pii/S1044580320321653. doi:10.1016/j.matchar.2020.110694.

[54] Z. Wang, M. Zhang, Z. Liu, Y. Wang, W. Dong, S. Zhao, D. Sun, Biomimetic design strategy of complex porous structure based on 3D printing Ti-6Al-4V scaffolds for enhanced osseointegration, Materials & Design 218 (2022) 110721. URL: https://linkinghub.elsevier.com/retrieve/pii/S0264127522003434. doi:10.1016/j.matdes.2022.110721.

[55] A. Cheng, A. Humayun, D. J. Cohen, B. D. Boyan, Z. Schwartz, Additively manufactured 3D porous Ti-6Al-4V constructs mimic trabecular bone structure and regulate osteoblast proliferation, differentiation and local factor production in a porosity and surface roughness dependent manner, Biofabrication 6 (2014) 045007. URL: https://iopscience.iop.org/article/10.1088/1758-5082/6/4/045007. doi:10.1088/1758-5082/6/4/045007.

[56] J. Wang, X. Ni, Q. Sun, D. Zhang, L. Chen, X. Jin, H. Cheng, J. Wang, Y. Hong, J. Yang, Additively manufactured trabecular porous tantalum: Effects of annealing temperature and oxygen content on mechanical properties, Journal of Materials Research and Technology 35 (2025) 4055–4070. URL: https://linkinghub.elsevier.com/retrieve/pii/S2238785425002789. doi:10.1016/j.jmrt.2025.02.030.

[57] J. Yang, H. Gao, D. Zhang, X. Jin, F. Zhang, S. Zhang, H. Chen, X. Li, Static Compressive Behavior and Material Failure Mechanism of Trabecular Tantalum Scaffolds Fabricated by Laser Powder Bed Fusion-based Additive Manufacturing, International Journal of Bioprinting 8 (2021) 438. URL: https://accscience.com/journal/IJB/8/1/10.18063/ijb.v8i1.438. doi:10.18063/ijb.v8i1.438.

[58] S. Khademzadeh, J. Rocco, L. Biasiolo, N. De Marchi, P. F. Bariani, Design and Additive Manufacturing of Bone-Inspired NiTi Scaffolds, in: Beam Based Technologies 1, 2019.

[59] S. Raghavendra, A. Molinari, A. Cao, C. Gao, F. Berto, G. Zappini, M. Benedetti, Quasistatic compression and compressioncompression fatigue behavior of regular and irregular cellular biomaterials, Fatigue & Fracture of Engineering Materials & Structures 44 (2021) 1178–1194. URL: https://onlinelibrary.wiley.com/doi/10.1111/ffe.13422. doi:10.1111/ffe.13422.

[60] S. Yamada, H. Suzuki, K. Sawada, S. Okada, A. Nishimura, M. Todoh, Novel strut-based stochastic lattice biomimetically designed based on the structural and mechanical characteristics of cancellous bone, Materials & Design 251 (2025) 113657. URL: https://linkinghub.elsevier.com/retrieve/pii/S0264127525000772. doi:10.1016/j.matdes.2025.113657.

[61] S. Ghouse, S. Babu, K. Nai, P. A. Hooper, J. R. Jeffers, The influence of laser parameters, scanning strategies and material on the fatigue strength of a stochastic porous structure, Additive Manufacturing 22 (2018) 290–301. URL: https://linkinghub.elsevier.com/retrieve/pii/S2214860418301313. doi:10.1016/j.addma.2018.05.024.

[62] M. He, Y. Li, J. Yin, Q. Sun, W. Xiong, S. Li, L. Yang, L. Hao, Compressive performance and fracture mechanism of bio-inspired heterogeneous glass sponge lattice structures manufactured by selective laser melting, Materials & Design 214 (2022) 110396. URL: https://linkinghub.elsevier.com/retrieve/pii/S026412752200017X. doi:10.1016/j.matdes.2022.110396.

[63] B. Zluhan, S. Ramadurga Narasimharaju, A. Cholkar, K. Thomas, R. Raghavendra, E. S. Lopes, Design, defect analysis, compressive strength and surface texture characterization of Laser Powder Bed Fusion processed Ti6Al4V lattice structures, Journal of Materials Research and Technology 35 (2025) 2914–2933. URL: https://linkinghub.elsevier.com/retrieve/pii/S2238785425002327. doi:10.1016/j.jmrt.2025.01.232.

[64] M. Araya, M. Jaskari, T. Rautio, T. Guilln, A. Jrvenp, Assessing the compressive and tensile properties of TPMS-Gyroid and stochastic Ti64 lattice structures: A study on laser powder bed fusion manufacturing for biomedical implants, Journal of Science: Advanced Materials and Devices 9 (2024) 100663. URL: https://linkinghub.elsevier.com/retrieve/pii/S2468217923001326. doi:10.1016/j.jsamd.2023.100663.

[65] X. Yue, J. Shang, M. Zhang, B. Hur, X. Ma, Additive manufacturing of high porosity magnesium scaffolds with lattice structure and random structure, Materials Science and Engineering: A 859 (2022) 144167. URL: https://linkinghub.elsevier.com/retrieve/pii/S0921509322015477. doi:10.1016/j.msea.2022.144167.

[66] Y. Zhang, J. Yang, W. Wan, Q. Zhao, M. Di, D. Zhang, G. Liu, C. Chen, X. Sun, W. Zhang, H. Bian, Y. Liu, Y. Tian, L. Xue, Y. Dou, Z. Wang, Q. Li, Q. Yang, Evaluation of biological performance of 3D printed trabecular porous tantalum spine fusion cage in large animal models, Journal of Orthopaedic Translation 50 (2025) 185–195. URL: https://linkinghub.elsevier.com/retrieve/pii/S2214031X24001402. doi:10.1016/j.jot.2024.10.010.

[67] A. S. Bhuwal, Y. Pang, I. Maskery, I. Ashcroft, W. Sun, T. Liu, Creep Characterization of Inconel 718 Lattice Metamaterials Manufactured by Laser Powder Bed Fusion, Advanced Engineering Materials (2023) 2300643. URL: https://onlinelibrary.wiley.com/doi/10.1002/adem.202300643. doi:10.1002/adem.202300643.

[68] C. Gao, J. Shi, H. Tang, H. Tang, Z. Xiao, Y. Bi, Z. Liu, J. H. Rao, Mechanical properties and energy absorption capabilities of plate-based AlSi10Mg metamaterials produced by laser powder bed fusion, Journal of Materials Research and Technology 30 (2024) 3851–3862. URL: https://linkinghub.elsevier.com/retrieve/pii/S2238785424008871. doi:10.1016/j.jmrt.2024.04.114.

[69] V. Viale, J. Stavridis, A. Salmi, F. Bondioli, A. Saboori, Optimisation of downskin parameters to produce metallic parts via laser powder bed fusion process: an overview, The International Journal of Advanced Manufacturing Technology 123 (2022) 2159–2182. URL: https://link.springer.com/10.1007/s00170-022-10314-z. doi:10.1007/s00170-022-10314-z.

[70] B. Li, W. Zhang, W. Fu, F. Xuan, Laser powder bed fusion (L-PBF) 3D printing thin overhang walls of permalloy for a modified honeycomb magnetic-shield structure, Thin-Walled Structures 182 (2023) 110185. URL: https://linkinghub.elsevier.com/retrieve/pii/S0263823122007376. doi:10.1016/j.tws.2022.110185.

[71] J. C. Fox, S. P. Moylan, B. M. Lane, Effect of Process Parameters on the Surface Roughness of Overhanging Structures in Laser Powder Bed Fusion Additive Manufacturing, Procedia CIRP 45 (2016) 131–134. URL: http://linkinghub.elsevier.com/retrieve/pii/S2212827116006429. doi:10.1016/j.procir.2016.02.347.

[72] M. Shange, I. Yadroitsava, A. Du Plessis, I. Yadroitsev, Roughness and Near-Surface Porosity of Unsupported Overhangs Produced by High-Speed Laser Powder Bed Fusion, 3D Printing and Additive Manufacturing 9 (2022) 288–300. URL: https://www.liebertpub.com/doi/10.1089/3dp.2020.0097. doi:10.1089/3dp.2020.0097.

[73] Z. Wu, S. P. Narra, A. Rollett, Exploring the fabrication limits of thin-wall structures in a laser powder bed fusion process, The International Journal of Advanced Manufacturing Technology 110 (2020) 191–207. URL: https://link.springer.com/10.1007/s00170-020-05827-4. doi:10.1007/s00170-020-05827-4.

[74] A. Gaikwad, F. Imani, P. Rao, H. Yang, E. Reutzel, Design Rules and In-Situ Quality Monitoring of Thin-Wall Features

Made Using Laser Powder Bed Fusion, in: Volume 1: Additive Manufacturing; Manufacturing Equipment and Systems; Bio and Sustainable Manufacturing, American Society of Mechanical Engineers, Erie, Pennsylvania, USA, 2019, p. V001T01A039. doi:10.1115/MSEC2019-3035.

[75] P. R. Gradl, C. S. Protz, K. Zagorski, V. Doshi, H. McCallum, Additive Manufacturing and Hot-fire Testing of Bimetallic GRCop-84 and C-18150 Channel-Cooled Combustion Chambers Using Powder Bed Fusion and Inconel 625 Hybrid Directed Energy Deposition, in: AIAA Propulsion and Energy 2019 Forum, American Institute of Aeronautics and Astronautics, Indianapolis, IN, 2019. URL: https://arc.aiaa.org/doi/10.2514/6.2019-4390. doi:10.2514/6.2019-4390.

[76] A. H. Seltzman, S. J. Wukitch, Precipitate Size in GRCop-42 and GRCop-84 Cu-Cr-Nb Alloy Gas Atomized Powder and L-PBF Additive Manufactured Material, Fusion Science and Technology 79 (2023) 503–516. URL: https://www.tandfonline.com/doi/full/10.1080/15361055.2022.2147765. doi:10.1080/15361055.2022.2147765.

[77] K. Morshed-Behbahani, A. Aliyu, D. P. Bishop, A. Nasiri, Additive manufacturing of copper-based alloys for high-temperature aerospace applications: A review, Materials Today Communications 38 (2024) 108395. URL: https://linkinghub.elsevier.com/retrieve/pii/S2352492824003751. doi:10.1016/j.mtcomm.2024.108395.

[78] G. Demeneghi, B. Barnes, P. Gradl, J. R. Mayeur, K. Hazeli, Size effects on microstructure and mechanical properties of additively manufactured copperchromiumniobium alloy, Materials Science and Engineering: A 820 (2021) 141511. URL: https://linkinghub.elsevier.com/retrieve/pii/S0921509321007802. doi:10.1016/j.msea.2021.141511.

[79] D. S. Scannapieco, J. J. Lewandowski, R. B. Rogers, D. L. Ellis, In-Situ Alloying of GRCop-42 via Additive Manufacturing: Precipitate Analysis (2020). URL: https://ntrs.nasa.gov/citations/20205003857.

[80] D. Scannapieco, Exploration and Modeling of In Situ Alloying via Additive Manufacturing for Dispersion Strengthened Copper Alloys, Ph.D. thesis, ???? URL: https://www.proquest.com/docview/3066120612?accountid=12725&sourcetype=Dissertations%20&%20Theses.

[81] S. Sahoo, M. M. Keleshteri, J. R. Mayeur, K. Hazeli, Stress localization investigation of additively manufactured GRCop-42 thin-wall structure, Thin-Walled Structures 201 (2024) 112022. URL: https://linkinghub.elsevier.com/retrieve/pii/S0263823124004658. doi:10.1016/j.tws.2024.112022.

[82] A. P. Thompson, H. M. Aktulga, R. Berger, D. S. Bolintineanu, W. M. Brown, P. S. Crozier, P. J. In 'T Veld, A. Kohlmeyer, S. G. Moore, T. D. Nguyen, R. Shan, M. J. Stevens, J. Tranchida, C. Trott, S. J. Plimpton, LAMMPS - a flexible simulation tool for particle-based materials modeling at the atomic, meso, and continuum scales, Computer Physics Communications 271 (2022) 108171. URL: https://linkinghub.elsevier.com/retrieve/pii/S0010465521002836. doi:10.1016/j.cpc.2021.108171.

[83] M. Miller, E. Berthier, 3D Bidisperse Granular STL File, 2022.

[84] M. A. Klatt, J. Kim, S. Torquato, Cloaking the underlying long-range order of randomly perturbed lattices, Physical Review E 101 (2020) 032118. URL: https://link.aps.org/doi/10.1103/PhysRevE.101.032118. doi:10.1103/PhysRevE.101.032118.

[85] C. E. Maher, K. A. Newhall, Characterizing the hyperuniformity of disordered network metamaterials, Physical Review E 111 (2025) 065420. URL: https://link.aps.org/doi/10.1103/l5hk-kwyn. doi:10.1103/l5hk-kwyn, publisher: American Physical Society.

[86] CloudCompare (version 2.1) [GPL software], 2024. URL: cloudcompare.org.

[87] M. Alns, J. Blechta, J. Hake, A. Johansson, B. Kehlet, A. Logg, C. Richardson, J. Ring, M. E. Rognes, G. N. Wells, The FEniCS Project Version 1.5, Archive of Numerical Software 3 (2015). URL: https://journals.ub.uni-heidelberg.de/index.php/ans/article/view/20553. doi:10.11588/ans.2015.100.20553.

[88] A. Logg, K.-A. Mardal, G. Wells (Eds.), Automated Solution of Differential Equations by the Finite Element Method: The FEniCS Book, volume 84 of *Lecture Notes in Computational Science and Engineering*, Springer, Berlin, Heidelberg, 2012. URL: https://link.springer.com/10.1007/978-3-642-23099-8. doi:10.1007/978-3-642-23099-8.

[89] A. Logg, G. N. Wells, DOLFIN: Automated finite element computing, ACM Trans. Math. Softw. 37 (2010) 20:1–20:28. URL: https://dl.acm.org/doi/10.1145/1731022.1731030. doi:10.1145/1731022.1731030.

[90] M. S. Alns, A. Logg, K. B. lgaard, M. E. Rognes, G. N. Wells, Unified form language: A domain-specific language for weak formulations of partial differential equations, ACM Trans. Math. Softw. 40 (2014) 9:1–9:37. URL: https://dl.acm.org/doi/10.1145/2566630. doi:10.1145/2566630.

[91] Y. Lee, M. Kirka, R. Dinwiddie, N. Raghavan, J. Turner, R. Dehoff, S. Babu, Role of scan strategies on thermal gradient and solidification rate in electron beam powder bed fusion, Additive Manufacturing 22 (2018) 516–527. URL: https://linkinghub.elsevier.com/retrieve/pii/S2214860417302439. doi:10.1016/j.addma.2018.04.038.

[92] C. Ledford, M. Tung, C. Rock, T. Horn, Real time monitoring of electron emissions during electron beam powder bed fusion for arbitrary geometries and toolpaths, Additive Manufacturing 34 (2020) 101365. doi:10.1016/j.addma.2020.101365.

[93] J. Ahrens, B. Geveci, C. Law, ParaView: An End-User Tool for Large Data Visualization, Visualization Handbook, Elsevier, 2005.

[94] M. A. Buhairi, F. M. Foudzi, F. I. Jamhari, A. B. Sulong, N. A. M. Radzuan, N. Muhamad, I. F. Mohamed, A. H. Azman, W. S. W. Harun, M. S. H. Al-Furjan, Review on volumetric energy density: influence on morphology and mechanical properties of Ti6Al4V manufactured via laser powder bed fusion, Progress in Additive Manufacturing 8 (2023) 265–283. URL: https://link.springer.com/10.1007/s40964-022-00328-0. doi:10.1007/s40964-022-00328-0.

[95] A. El Hassanin, A. T. Silvestri, F. Napolitano, D. Borrelli, A. Caraviello, A. Astarita, Investigation of the laser-related parameters in Laser-Powder Bed Fusion of Inconel 718-Cu blends at fixed Volumetric Energy Density, Journal of Manufacturing Processes 99 (2023) 456–468. URL: https://linkinghub.elsevier.com/retrieve/pii/S1526612523005534. doi:10.1016/j.jmapro.2023.05.068.

[96] A. Marques, . Cunha, M. R. Silva, M. I. Osendi, F. S. Silva, . Carvalho, F. Bartolomeu, Inconel 718 produced by laser powder bed fusion: an overview of the influence of processing parameters on microstructural and mechanical properties, The International Journal of Advanced Manufacturing Technology 121 (2022) 5651–5675. URL: https://link.springer.com/10.1007/s00170-022-09693-0. doi:10.1007/s00170-022-09693-0.

[97] W. Guo, B. Feng, Y. Yang, Y. Ren, Y. Liu, H. Yang, Q. Yang, L. Cui, X. Tong, S. Hao, Effect of laser scanning speed on the microstructure, phase transformation and mechanical property of NiTi alloys fabricated by LPBF, Materials & Design 215 (2022) 110460. URL: https://linkinghub.elsevier.com/retrieve/pii/S0264127522000818. doi:10.1016/j.matdes.2022.110460.

[98] A. Kumar Ramavajjala, T. R. Dandekar, R. K. Khatirkar, C. Joshi, R. N. Chouhan, A. Agnihotri, A review on the correlation between microstructure, heat treatment and mechanical properties of additively manufactured AlSi10Mg by LPBF, Critical Reviews in Solid State

and Materials Sciences (2024) 1–36. URL: `https://www.tandfonline.com/doi/full/10.1080/10408436.2024.2414012`. doi:`10.1080/10408436.2024.2414012`.

[99] Y.-j. Xie, H.-c. Yang, X.-b. Wang, L. Zhao, C.-j. Kuang, W. Han, Control of wall thickness and surface morphology of tungsten thin wall parts by adjusting selective laser melting parameters, Journal of Iron and Steel Research International 26 (2019) 182–190. URL: `http://link.springer.com/10.1007/s42243-019-00234-w`. doi:`10.1007/s42243-019-00234-w`.

[100] T. Puttonen, S. Chekurov, J. Kuva, R. Bjrkstrand, J. Partanen, M. Salmi, Influence of feature size and shape on corrosion of 316L lattice structures fabricated by laser powder bed fusion, Additive Manufacturing 61 (2023) 103288. URL: `https://linkinghub.elsevier.com/retrieve/pii/S2214860422006777`. doi:`10.1016/j.addma.2022.103288`.

[101] M.-A. de Pastre, Y. Quinsat, C. Lartigue, Direct additive manufactured beam shape defect identification from computed tomography and modal decomposition, in: Direct additive manufactured beam shape defect identification from computed tomography and modal decomposition."Joint Special Interest Group meeting between euspen and ASPE Advancing Precision in Additive Manufacturing., 2021.

[102] B.-L. Chua, H.-J. Lee, D.-G. Ahn, Estimation of Effective Thermal Conductivity of Ti-6Al-4V Powders for a Powder Bed Fusion Process Using Finite Element Analysis, International Journal of Precision Engineering and Manufacturing 19 (2018) 257–264. URL: `http://link.springer.com/10.1007/s12541-018-0030-2`. doi:`10.1007/s12541-018-0030-2`.

[103] L. C. Wei, L. E. Ehrlich, M. J. Powell-Palm, C. Montgomery, J. Beuth, J. A. Malen, Thermal conductivity of metal powders for powder bed additive manufacturing, Additive Manufacturing 21 (2018) 201–208. URL: `https://linkinghub.elsevier.com/retrieve/pii/S2214860417306231`. doi:`10.1016/j.addma.2018.02.002`.

[104] G. Li, R. Ganeriwala, D. Herzog, K. Bartsch, W. King, Numerical and experimental investigation of the geometry dependent layer-wise evolution of temperature during laser powder bed fusion of Ti6Al4V, Progress in Additive Manufacturing 8 (2023) 961–975. URL: `https://link.springer.com/10.1007/s40964-022-00370-y`. doi:`10.1007/s40964-022-00370-y`.

[105] D. Wang, Y. Yang, Z. Yi, X. Su, Research on the fabricating quality optimization of the overhanging surface in SLM process, The International Journal of Advanced Manufacturing Technology 65 (2013) 1471–1484. URL: `http://link.springer.com/10.1007/s00170-012-4271-4`. doi:`10.1007/s00170-012-4271-4`.

[106] X. Zhao, A. Liang, M. Bellin, N. W. Bressloff, Effects of process parameters and geometry on dimensional accuracy and surface quality of thin strut heart valve frames manufactured by laser powder bed fusion, The International Journal of Advanced Manufacturing Technology 133 (2024) 543–557. URL: `https://link.springer.com/10.1007/s00170-024-13627-3`. doi:`10.1007/s00170-024-13627-3`.

[107] S. S. Xue, J. W. Barlow, Models for the Prediction of the Thermal Conductivities of Powders (1991). URL: `http://hdl.handle.net/2152/64283`.

[108] S. Yagi, D. Kunii, N. Wakao, Studies on axial effective thermal conductivities in packed beds, AIChE Journal 6 (1960) 543–546. URL: `https://aiche.onlinelibrary.wiley.com/doi/10.1002/aic.690060407`. doi:`10.1002/aic.690060407`.

[109] M. Liu, L. N. Chiu, H. Shen, X. Fang, Z. Tao, A. Huang, C. Davies, X. Wu, W. Yan, Effective thermal conductivities of metal powders for additive manufacturing, Powder Technology 401 (2022) 117323. URL: `https://linkinghub.elsevier.com/retrieve/pii/S0032591022002170`. doi:`10.1016/j.powtec.2022.117323`.

[110] H. Zhang, Y. Zhao, F. Wang, D. Li, A 3D discrete element-finite difference coupling model for predicting the effective thermal conductivity of metal powder beds, International Journal of Heat and Mass Transfer 132 (2019) 1–10. URL: `https://linkinghub.elsevier.com/retrieve/pii/S0017931018344314`. doi:`10.1016/j.ijheatmasstransfer.2018.11.118`.

[111] D. Moser, S. Pannala, J. Murthy, Computation of Effective Thermal Conductivity of Powders for Selective Laser Sintering Simulations, Journal of Heat Transfer 138 (2016) 082002. URL: `https://asmedigitalcollection.asme.org/heattransfer/article/doi/10.1115/1.4033351/454616/Computation-of-Effective-Thermal-Conductivity-of`. doi:`10.1115/1.4033351`.